Time-Resolved Imaging of Flame Kernels: Laser Spark Ignition of $H_2/O_2/Ar$ Mixtures

T. A. SPIGLANIN, A. MCILROY, E. W. FOURNIER, R. B. COHEN, and J. A. SYAGE

The Aerospace Corporation, P.O. Box 92957/M5-754, Los Angeles, California 90009-2957

The shape and structure of developing flame kernels in laser-induced spark ignited hydrogen/air mixtures is investigated as a function of gas composition and time. Using planar laser-induced fluorescence (PLIF) to measure the spatial distribution of OH radicals produced inside the reaction zone, we have recorded the evolution of the nascent flame kernel in a series of images following the laser-induced spark. This series provides the rate of flame growth, the evolution of the flame shape, and the intensity of the PLIF signal as a function of time for both igniting flames and nonignition events. The reaction zones grow quickly at early times, but slowly decrease in propagation rate as the energy density within the flame kernel decreases. A distinct anisotropy is observed in the expanding spark and flame kernel. At short times ($t < 100$ μs), a toroidal shape is observed similar to that seen previously for electrode-spark ignitions and for laser ignitions in methane/air. There is also a tendency for the flame to grow back toward the ignition laser. Successful ignitions appear virtually identical to failed ignitions during the first 100 μs. Significant differences, notably in intensity, appear between 100 and 500 μs following the spark. These observations imply that early flame kernel growth is dominated by gas motion induced by the short-duration spark. The ultimate fate of an ignition lies with the chemistry of the reactions which determines whether the gas undergoes a transition from hot plasma to propagating flame.

INTRODUCTION

Spark ignition of gases has a wide range of applications that include, for example, internal combustion engines, supersonic ramjets and improved fire/ignition suppression systems [1–5]. Significant advances in these technologies are currently limited by a poor understanding of the microscopic details of ignition. Our research is aimed at explaining the mechanisms of ignition during its earliest stages, emphasizing the interplay between chemistry and fluid mechanics of the developing flame kernel. The focus of this paper is the physical shape and development of the flame kernel during the first 3 ms. These properties depend critically on both chemical kinetics and fluid dynamics, thus experimental measurements should provide a good foundation for theoretical developments.

Spark ignition involves the deposition of a localized source of energy in a flammable gas mixture to produce a small plasma [6–10]. The plasma energy propagates by initiating exothermic chemistry involving the fuel and oxidizer, resulting in a local over pressure and elevated temperature in the evolving gas kernel. This is followed by a quasiadiabatic expansion (relaxation) that leaves the gas kernel in a state of high temperature and low density [11–15]. This rapid expansion results in a shock wave propagating outward from the hot gas kernel. The intensity of the shock wave depends on the duration, volume, and energy of the initial spark. The energetic species react with other molecules within the spark volume (kernel) and at the boundary between the energetic kernel and the surrounding gas (i.e., the flame front), liberating yet more energy. Chemistry at the boundary layer promotes further flame kernel growth that propagates outward until the flame kernel either dies out (if an insufficient amount of initial energy is supplied for the specific gas composition) or develops into a self-sustained freely propagating flame. The early flame kernel is fragile because the surface area of the expanding flame kernel increases rapidly (i.e., flame stretch). The heat generated by combustion must increase proportionately to maintain the flame ignition temperatures, otherwise, the flame extinguishes. As the flame kernel expands and the flame front becomes more planar relative to the flame thickness, propagation becomes more stable. Since flame extinction is most likely to occur in the initial stages of ignition, a detailed

0010-2180/95/$9.50
SSDI 0010-2180(94)00278-Z

COMBUSTION AND FLAME 102:310–328 (1995)

Published by Elsevier Science Inc.

understanding of the fluid dynamics and reaction mechanics for ignition onset is vital for enhancing ignition efficiency or for developing new methods of fire suppression.

The strong coupling between physical and chemical processes that leads to flame formation makes ignition exceptionally difficult to understand. There have been numerous attempts to model ignition by numerical simulations. Beginning in 1974, these calculations started combining chemical kinetics with dynamical models for flame propagation. The earliest of these used a reaction mechanism for the hydrogen/oxygen system consisting of 11 steps [6]. Increased computational speed has enabled more complex reaction mechanisms to be included to accurately describe the chemistry of ignition phenomena [7–9, 11]. Despite these advances, the majority of simulations were confined to a one-dimensional geometry, most often taken as the radial coordinate of a cylindrical geometry.

A recent calculation by Kono et al. added a second spatial dimension (length) to the simulation but suppressed chemical reactions [12]. The resulting calculation therefore reasonably represented the physical development of a cylindrical hot gas kernel with finite length imbedded in an inert gas. The development of this hot kernel was followed as a function of time to determine the forces that influence the evolution of a nascent flame kernel in a flammable gas. About 2 μs after insertion of the hot, ellipsoidal gas kernel, a shock wave rapidly propagates outward, followed by a slower development of the residual hot gas. By 100 μs, the residual gas clearly becomes toroidal and continues to propagate outward in this manner until the kernel dissipates. Comparisons between the calculated temperature profiles and measured Schlieren photographs of hot gas kernels produced between two electrodes in air and in propane/air mixtures show good qualitative agreement. Examination of other Schlieren images of ignition kernels shows a similarity to the hot gas kernels at early times [12]. Recently Warnatz and coworkers reported a two-dimensional numerical study of laser-induced ignition in hydrogen–oxygen mixtures that incorporates chemical reactions [15]. The energy deposition was modeled as a continuous source for a fixed period of time and, therefore, is not strictly representative of the spark ignition conditions employed in this work. Nonetheless, numerical techniques for modeling ignition are becoming more realistic, which should improve the convergence and coordination of experimental and theoretical work in this area. Experimental data describing the early time evolution of combustion are indispensable for validating and guiding these theoretical efforts.

Since the coupling between chemical and physical forces is central to the development of flame kernels, probes are required that provide time, space and chemical species resolved data. The small size (< 5 mm in diameter) and relatively delicate nature of flame kernels require the use of noninvasive optical probes. Planar laser induced fluorescence (PLIF) imaging has been used extensively over the years as a detailed probe of flame properties [16–20]. The majority of work has examined the spatial properties (e.g., boundary layers) of steady-state flames. Far less progress has been made in imaging ignition processes. Wolfrum, Maly, and coworkers recorded PLIF images of a spark-plug-ignited internal-combustion simulator using acetaldehyde as a fluorescence tracer [19]. Seitzman et al. reported PLIF images of OH density for laser spark ignited mixtures of methane/air [20].

Our work on the time-evolving properties of flame initiation also makes use of laser-induced ignition. The advantages of laser initiation are that it is a clean and remote source of energy, permits unobstructed optical access to the flame kernel, and eliminates adverse effects of electrode discharge ignition (i.e., surface catalysis or poisoning, disruption of the flame kernel and gas flow, etc.). Ronney has recently reviewed the topic of laser versus conventional ignition of flames and categorized different types of laser ignition [21]. A laser can deposit energy into a gas by any of several mechanisms including resonant and nonresonant multiphoton ionization, optical absorption, and photodissociation [5, 9, 20–31]. In this work we rely on a focused laser pulse to induce a spark discharge by nonresonant multiphoton ionization and inverse Bremsstrahllung radiative absorption. The

properties of laser spark ignition are expected to differ considerably from resonant photochemical ignition although no systematic studies of time evolving properties have been made in comparable combustion mixtures. Miziolek and coworkers have shown significant enhancements in ignition efficiency by resonant multiphoton excitation of O and H-atom intermediates in H_2/O_2 flames [26–28]. Other groups have also observed photochemical enhancements of combustion [29–31]. Laser-induced spark ignition, as employed here, should more closely resemble traditional electric discharge ignition than resonance-enhanced photochemical ignition.

In earlier work, we explored the use of picosecond and nanosecond laser spark ignition for measuring minimum ignition energies and for understanding the macroscopic flow dynamic properties of flame growth [22]. Laser ignition schemes that use focused laser beams, similar to the apparatus described in this report, can deposit energy into a very small volume, but the composition of the initial flame kernel and its spatial extent are difficult to predict. Time-resolved imaging techniques can provide detailed characterization of these initial conditions. The experimental data combined with modeling effort should help to improve ignition systems, guide future theoretical efforts, and simulate novel ideas for initiating and enhancing combustion or for suppressing combustion.

This report details our measurements using PLIF imaging techniques of the spatial development of nascent flame kernels that result from short-duration laser-induced sparks in $H_2/O_2/Ar$ mixtures. We report time-resolved results for several fuel/oxidizer ratios and dilutions from flame ignition to full propagation or extinction. Initial flame growth from laser ignition resembles in some ways the process of electric spark ignition; however, the initial stages of energy deposition differ considerably. An important problem discussed by Ronney [21] is understanding the relationship of laser (and electric discharge) spark size relative to the critical radius of the ignition volume or minimum flame kernel size for varying fuel/oxidizer mixtures. The present work, in addition to providing time-resolved images of the combustion process, also looks directly at the early time spatial evolution of the laser spark.

EXPERIMENTAL

The experimental apparatus used in these studies is sketched in Fig. 1. There are five key subsystems: the gas flow control and burner, the ignition laser, the probe laser, the camera, and the timing and data acquisition system.

Three Tylan FC-261V flow controllers are used to adjust the flow of 25% hydrogen in argon (Spectra Gases research grade or Linde), argon (Linde) and oxygen (Linde) gases. These are mixed in a manifold and then directed through the center of an atmospheric pressure flat flame burner assembly (McKenna Products, Inc.) with a porous bronze head. A second flow of argon is controlled by a Tylan FC-261V flow controller and passes throu the outer shield ring of the burner assembly. Argon diluent is used rather than nitrogen in order to simplify the chemical reaction mechanism by eliminating the possibility of secondary nitrogen chemistry. The flow controllers are calibrated for each gas or mixture against a standard flow meter. Because the hydrogen is diluted in argon, changes in the hydrogen/argon flow rate cause the oxygen/argon ratio to vary. We set the ratio of oxygen to total argon flow equal to the oxygen/nitrogen ratio in air, thus producing a "synthetic air." The gases exit the burner with a velocity of approximately 10.4 cm/s. This velocity is significantly less than the measured flame speeds in the incipient flame kernels. On the time scales investigated here (< 4 ms), the gas is approximately still. The flow through the outer ring of the burner matches the burner flow rate to reduce the effects of shear at the edges of the flammable gas flow. Prior to ignition, all mixtures are at a pressure of 1 atm and temperature of 298 K.

A small Q-switched Nd:YAG laser (Laser Photonics MYL-100) creates the ignition spark This laser produces a single, 8-ns pulse at 10 nm with a beam diameter of 3 mm and an energy of approximately 22 mJ. This laser is fired by external command from custom timing

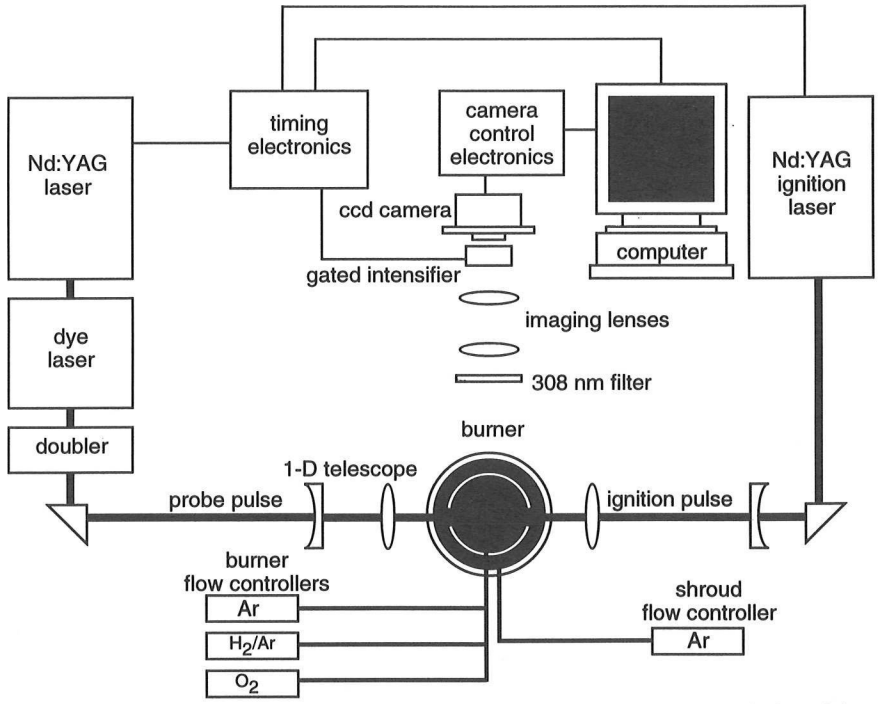

Fig. 1. Diagram of the experimental apparatus used in this study. The relative timing of the laser pulses and camera shutters is detailed in Fig. 2. Refer to the text for other details.

circuitry with a delay between the external pulse and the output laser pulse of approximately 215 ms with approximately 2 μs jitter. To achieve a sufficiently tight focus for laser breakdown, the laser pulse diameter is first expanded (-75 mm focal length diverging lens) and then focused (75 mm focal length converging lens) to a point approximately 1.5 cm above the center of the burner surface. The focused beam has a beam waist of 0.013 mm diameter and a focusing length (i.e., diameter less than twice the beam waist) of 0.5 mm. This arrangement reliably produces a spark in air with each laser pulse. Spark energies are measured using the method described in our earlier work [22]. A Laser Precision RjP735 energy probe monitors the energy of the beam by sampling the reflected beam (approximately 10% total reflection) from a quartz window positioned between the laser and the diverging lens. A second Laser Precision RjP735 probe measures the energy of the transmitted laser light. The energy dissipated in the spark is obtained by subtracting the two calibrated probe signals. The energy deposited into a spark varied widely, from 1 to over 19 mJ with most sparks falling in the 11–14 mJ range. For these studies, only results for laser-induced spark energies of 11–14 mJ were retained.

The probe laser system consists of a Quanta Ray DCR-2 Nd:YAG laser, a PDL-2 dye laser, and a WEX wavelength extender and is operated at 283 nm, 8–9 mJ/pulse, 7 ns duration, 10 Hz repetition rate. A one-dimensional telescope is used to shape the probe pulse. The telescope consists of a diverging cylindrical lens (-75 mm focal length) to expand the beam in the vertical direction, and a spherical lens (300 mm focal length) to collimate the vertical expansion while mildly focusing the beam in the horizontal direction. The resulting beam is approximately 2 cm tall and 250 μm wide and counterpropagates with the spark laser over the burner assembly, parallel to the image plane of the camera system. The laser wavelength was tuned to the $Q1(5)$ line in the (1,0) vibrational band of the $A^2\Sigma^+ \leftarrow X^2\Pi$ transition in OH by maximizing the OH laser-induced fluorescence intensity (LIF) from a small natural gas/air flame. This optimization is performed immediately prior to capturing PLIF images.

The camera system consists of a Photometrics CC200 camera controller, a CE200 electronics unit, and a CH220 camera head. The camera contains a thermoelectrically cooled Thompson CSF TH7882CDA grade A charge-coupled device (CCD) sensor. The input window of the sensor is optically bonded to a fiber-optic bundle that protrudes through the front face of the camera housing. A Varo, Inc. model 5772 Type I UV sensitive image intensifier tube with fiberoptic output window of 18-mm diameter mates to the camera's input window to form a highly sensitive, ultraviolet-capable imaging camera. A power supply, designed for pulsed image intensifier tubes by K & M electronics (model 2084), supplies the voltages required by the intensifier tube. This supply provides a gate pulse having a rise time of less than 100 ns that enables the intensifier to operate only when commanded. A 200 ns wide gate is used to collect data. Spherical quartz optics image the LIF signal onto the front of the intensifier tube through an interference filter (Acton) with a bandpass of 25 nm and a center wavelength of 308 nm, separating the 1-1 and 0-0 fluorescence from the 1-0 emission and scattered laser light.

The timing system supplies TTL pulses to prepare the camera system for image acquisition, to gate the image intensifier tube, and to trigger the ignition laser. Figure 2 shows the relative positions of these pulses, each timed with better than 0.1 ns accuracy relative to the 10-Hz clock used by the probe laser system. The delay between any two pulses can be independently varied to measure images for different delays between ignition and probe lasers. A typical sequence that records one image proceeds as follows: First the CCD array is cleared of accumulated charge and the camera shutter opened. The timing circuitry then initiates firing of the ignition laser, activates the intensifier, closes the camera shutter, and quickly reads the charge accumulated on the CCD into an image buffer in the CC200. A microcomputer controls the experiments through a IEEE 488 bus and coordinates transfers of desired images from the image buffer of the CC200 camera controller to the hard disk for later use. Prior to transfer, the CC200 subtracts a dark image from the new image, then normalizes the result by a flat-field frame. The images are then available for further processing including false-color or contour plots for analysis and presentation.

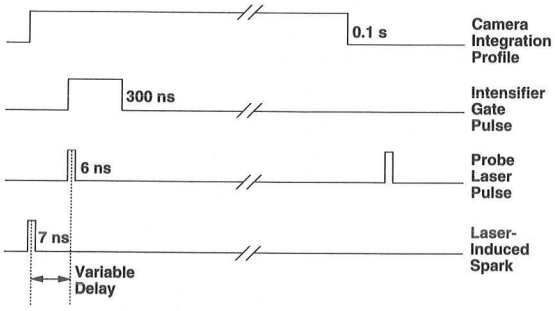

Fig. 2. Timing diagram for PLIF imaging of spark ignition events. The contour intervals are linear; all images are plotted on the same relative intensity scale. The camera integrates its image for more than 0.1 but the intensifier gate provides an optical shutter that prevents any image from accumulating on the CCD sensor except during the gate pulse. The gate pulse eclipses the probe laser that operates at 10 Hz. All electronic components are timed relative to the probe laser pulse frequency.

The dependence of detected fluorescence intensity on species concentration, which we briefly review here, has been treated many times in the past [18]. For PLIF imaging, the spatially resolved fluorescence intensity $I(x,y)$ can be related to the OH radical concentration profile $N_{OH}(x,y)$ by the expression

$$I(x,y) = \Omega N_{OH}(x,y) f_{v,J}(T) \Phi(P,T,x,y) \quad (1)$$

$$\Phi(P,T,x,y) = \frac{k_r}{k_r + \sum_i k_{q,i}(P,T) N_i(x,y)}, \quad (2)$$

where Ω is the detection efficiency which encompasses the probe laser pulse energy, detector field of view and detector gain, $f_{v,J}(T)$ is the fractional population of the v,J state of OH being probed by LIF, and $\Phi(P,T,x,y)$ is the fluorescence quantum yield, where k_r is the radiative rate constant and $k_{q,i}(P,T)$ is the fluorescence quenching rate constant for collision of OH with species i of density $N_i(x,y)$. Every effort was made to render the fluorescence images $I(x,y)$ a reliable measure of the $N_{OH}(x,y)$ spatial profile. The detect gain and field of view were maintained constant throughout the experiment. The probe laser pulse energy was kept constant to within

the pulse-to-pulse fluctuations of 10%. The $Q1(5)$ line in the (1,0) vibrational band was chosen to minimize the variation of $f_{v,J}(T)$ with T at high temperatures. To permit comparisons between different ignition events, only PLIF images resulting from a narrow range of spark energies (11–14 mJ) are reported. The proportionality between $I(x, y)$ and $N_{OH}(x, y)$ is probably most affected by the fluorescence quenching rates. Because of gradients in pressure, temperature, and chemical species, the fluorescence quenching rate may vary across the ignition kernel giving a nonlinear relationship between $I(x, y)$ and $N_{OH}(x, y)$. The PLIF images are still a reliable measure of the shape of the OH concentration, but the intensity scale may not be strictly linear with concentration. A correction is not possible at this stage because it is not practical to determine simultaneously the instantaneous P, T, and N_i profiles. However, a modeling effort incorporating chemical kinetics and gas dynamics would provide this information, making it routine to correct for the fluorescence quenching effects.

The contour plots of PLIF images in this paper are reported using a linear contour interval. All images are plotted to the same relative intensity scale so that comparisons of images within and between figures can be made with regard to spatial structure and intensity. The uncertainty of the relative scale is about 20% for images within a figure and 20%–40% between figures due primarily to the variation of spark energy and probe energy for different ignition events (see above). Hence, these images should provide sufficient information to model the spatial and temporal evolution of an ignition kernel with regard to the OH concentration gradients and with regard to the relative OH concentrations for different ignition events.

Figure 3 demonstrates the reproducibility of the laser-induced spark ignition process as monitored by PLIF imaging. The four small panels show a complete data set for a 100-μs delay between the ignition and probe lasers with a 10% hydrogen in synthetic air mixture. The spark energies are as noted in the figure and all images are plotted on the same linear gray scale. The center panel displays the average of these four images. Several important characteristics of the experimental method are evident. First the qualitative shape of the images is highly reproducible from one ignition

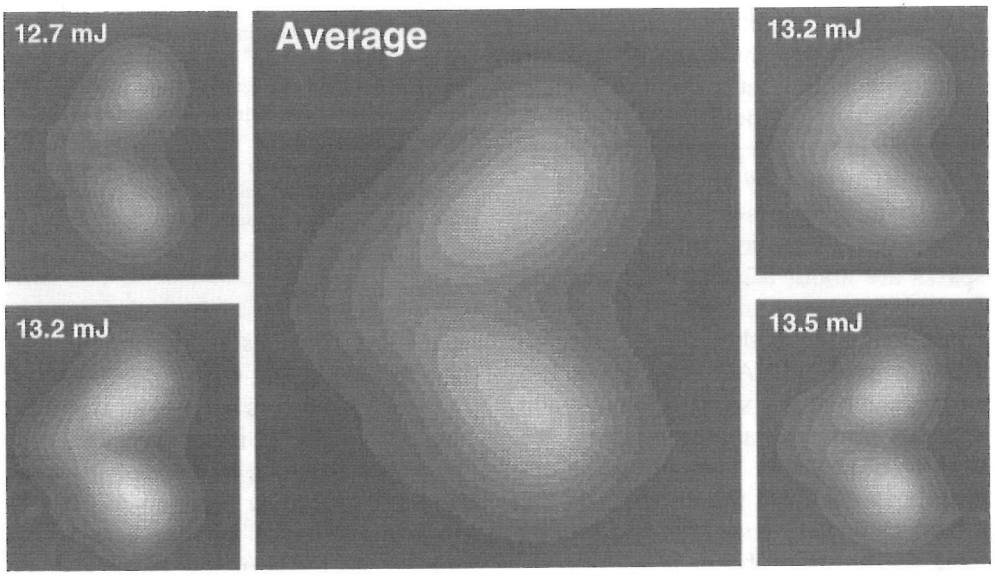

Fig. 3. A demonstration of the reproducibility of the laser-induced spark ignition process as monitored by PLIF imaging. The four small panels show a complete data set for a 100-μs delay between the ignition and probe lasers with a 10% hydrogen in synthetic air mixture. The spark energies are as noted in the figure and all images are plotted on the same linear gray scale where lighter areas represent higher OH concentrations.

event to the next. Thus we are confident that a series of images taken under identical conditions at varying delays from the ignition pulse provides a realistic picture of propagation of a single ignition event. Second, the reproducibility and signal-to-noise ratio to the data are sufficiently high that there is no significant advantage to averaging all collected images at a particular mixture and time delay. Indeed averaging could potentially lead to the loss of information if turbulent structures played an important role in the ignition process.

RESULTS

Laser-induced spark energies of about 10 mJ easily ignite a steady flame on the burner surface when the gas mixture contains 7% or more hydrogen diluted in synthetic air. Successful ignitions are evident by monitoring sustained temperature rises in the gases entering the exhaust flue, OH emission from the region immediately above the burner surface, and a rapid return of the exhaust gas temperature to ambient when the hydrogen gas flow is interrupted. Unsuccessful ignition attempts for mixtures with less than 7% hydrogen begin with temperature rises that persist for several seconds with rapid fluctuations followed by a precipitous drop, indicating extinction. Gas mixtures with less than 4% hydrogen (this is the lean flammability limit in air) exhibit only slight transient increases in temperature at the thermocouple probe in the exhaust flue. The laser-induced sparks formed by the ignition laser beam in nonflammable gases are examined by imaging the natural emission from the sparks. These sparks are about 0.2 mm wide and less than 0.7 mm long, approximately 0.1 mm wider and 0.2 mm longer than the confocal dimensions of the focused Nd:YAG laser beam. Images clearly show that the sparks elongate and often separate into several points along the path of the focused beam. The elongation appears to extend away from the direction of the incident laser beam with a well-defined leading edge facing the incoming beam in every case. In almost every case of separated centers, the intensity of the emission is greatest for the points closest to the source of the ignition laser beam. The first frame of Fig. 4 (3 μs delay) strongly resembles the results of the spark investigations and exemplifies the definition of the leading edge.

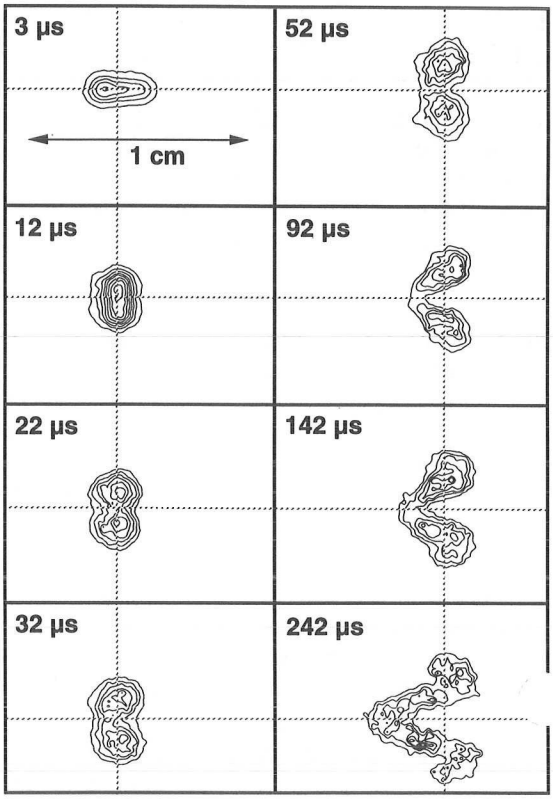

Fig. 4. Contour plots derived from PLIF images of nascent flame kernels in a mixture of 7% hydrogen in an oxygen/argon synthetic air atmosphere. The contour intervals are linear; all images are plotted on the same relative intensity scale. Each image is the result of a separate ignition event, assembled here to show the development of the nascent flame. Figure 3 demonstrates the reproducibility of the ignitions and validates this method. The laser used for ignition enters from the left and is focused approximately at the intersection of the lines superimposed on each frame. The contours are linear steps in OH PLIF signal, and the same scaling is used for each panel and for all subsequent figures.

Figure 4 displays a series of contour plots of single shot PLIF images of OH for several igniting flames in a mixture of 7% hydrogen in synthetic air. The ignition laser propagates from left to right, and the approximate location of the focus of this beam is indicated in each frame of Fig. 4. Because the probe las beam is effectively a sheet of light, the images represent two-dimensional cross sections through flame fronts that are expanding in

three dimensions. At the earliest times (3–12 μs), OH intensity emanates from the center of the spark volume and evolves rapidly into an ellipsoid. As time progresses, the ellipsoid becomes a toroid that surrounds the region where the spark occurred. The toroid continues to expand radially away from the spark center and persists to 300 μs, eventually dissipating at longer times.

At approximately 100 μs the flame develops a noticeable asymmetry along the axis of the ignition laser beam. This asymmetry continues to grow into a flame front that propagates backward with respect to the spark laser direction. The last image shown in Fig. 4 clearly exhibits this nascent flame front. In Fig. 5, images recorded with 10% hydrogen from 100 μs to 3.00 ms clearly demonstrate this effect and indicate no noticeable development of a flame front to encircle the other "side" of the spark region. By 600 μs, propagation back toward the ignition laser becomes the predominant feature of the flame front. The extent of the flame propagation back along the path of the ignition laser beam varies greatly from image to image for mixtures containing between 5% and 8% hydrogen. This corresponds to a range of gas compositions that are flammable but not readily ignitable by our laser pulse. At hydrogen concentrations above

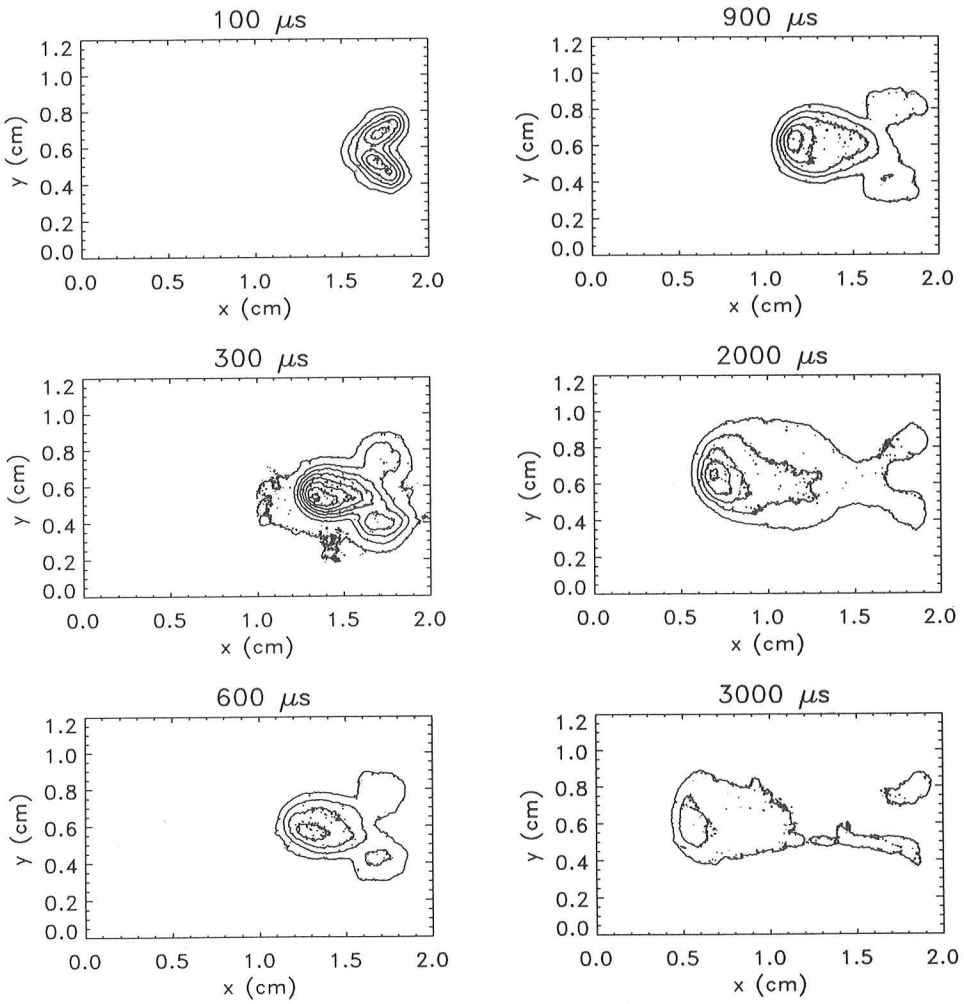

Fig. 5. Contour plots derived from PLIF images of flame kernels in a mixture of 10% hydrogen in an oxygen/argon synthetic air atmosphere. The contours are linear steps in OH PLIF signal, and the same scaling is used for each panel. See Figure 4 caption.

8%, the backward propagating flame front occurs reproducibly and predominates at long times. The preferential flame growth back toward the ignition laser is discussed further below. This phenomenon has been observed previously by Hanson and coworkers in PLIF imaging studies of a uv laser ignited methane/air mixture [20].

We investigate the effect of gas composition on the structure of nascent flames at several delays between the ignition and probe laser pulses. Remarkably all flame kernels recorded at early times (≤ 100 μs) for gas mixtures containing from 3% to 11% hydrogen exhibit similar behavior. Figure 6 displays contour plots of images obtained at 100 μs for mixtures containing 2%–8% hydrogen. The geometry of the flame kernel is virtually identical for all concentrations interrogated. The most noticeable difference between images recorded up to approximately 100 μs for flammable and nonflammable mixtures is the total OH laser-induced fluorescence intensity. Mixtures that support combustion show significantly more PLIF intensity than those that do not.

In contrast to the qualitative similarity of the images as function of hydrogen concentration at short times (≤ 100 μs), remarkably different behavior is seen at longer times. Figure 7 displays OH contour plots measured at 300 μs following ignition attempts in gas mixtures containing 3.4%–11% hydrogen. As evidenced in the first two frames of Fig. 7, the shapes of the kernels of hot gas are difficult to identify by 300 μs at concentrations below 7% hydrogen. By contrast, flame kernels in

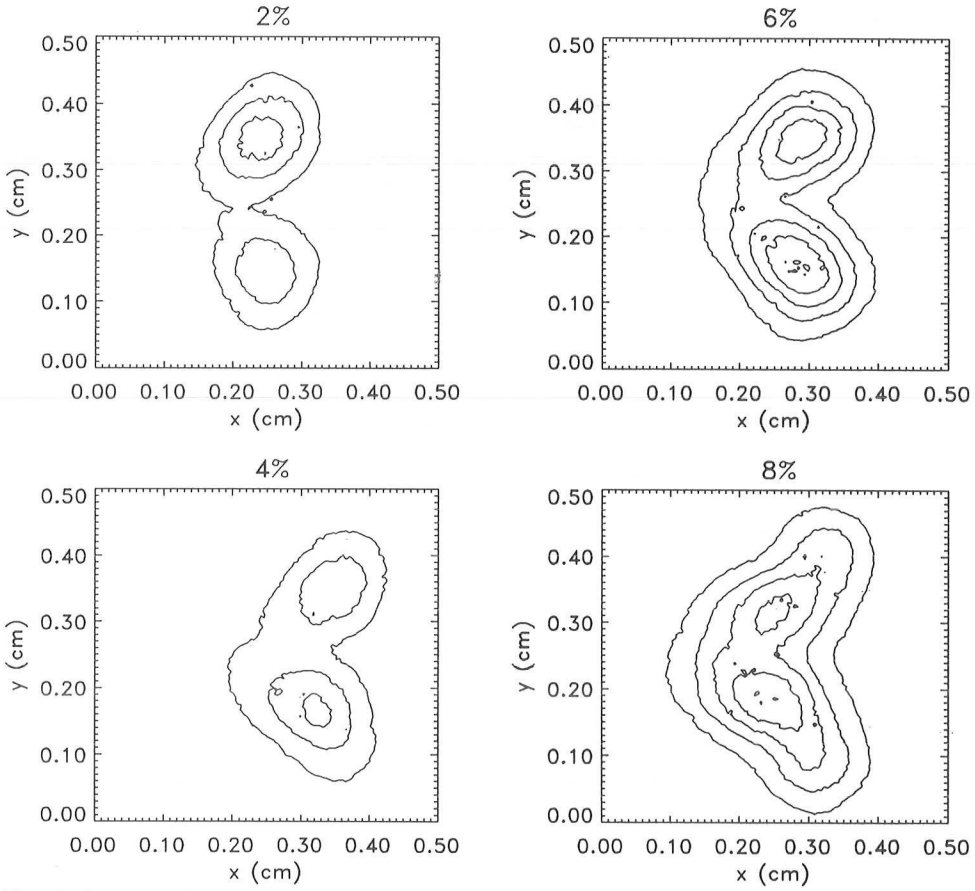

Fig. 6. Contour plots derived from OH PLIF images of laser-ignited mixtures of hydrogen in oxygen/argon synthetic air. The frames are labeled with the percentage of hydrogen gas in the mixture. These images were recorded at 100 μs following the laser-induced spark. Note that toroidal shapes of all kernels are very similar at this short time. The contours are linear steps in OH PLIF signal, and the same scaling is used for each panel.

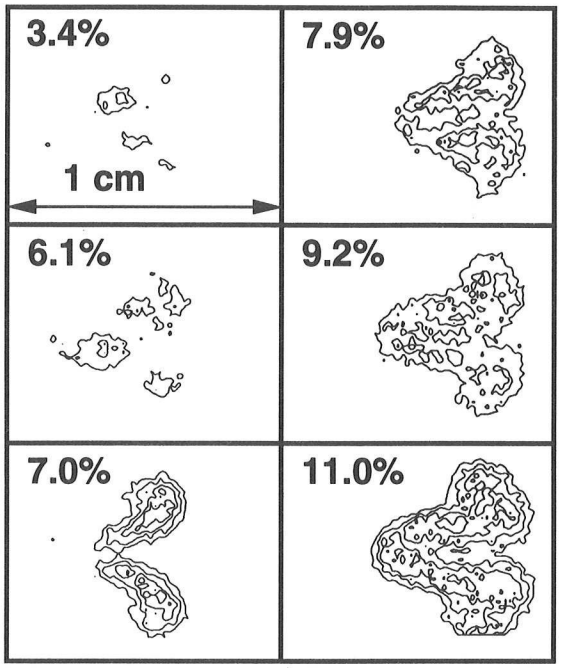

. 7. Contour plots derived from OH PLIF images of ..ser-ignited mixtures of hydrogen in oxygen/argon synthetic air. The frames are labeled with the percentage of hydrogen gas in the mixture. These images were recorded at 300 μs following the laser-induced spark. At hydrogen concentrations below 7%, gas mixtures fail to ignite the burner in our laser ignition experiments correlating well with short time behavior shown here. The contours are linear steps in OH PLIF signal, and the same scaling is used for each panel.

flammable mixtures continued to develop and are easily mapped by our imaging techniques. The series of images in Fig. 7 exemplify the difference between ignition attempts that succeed and those that fail. Comparing the image for 7% hydrogen (nominally ignitable) with that for 11% hydrogen indicates no significant differences in the distance between the zones where OH is located and the initial spark, particularly in the diameter of the toroidal shape. As Fig. 7 demonstrates, by 300 μs only at hydrogen concentrations that lead to successful ignition (7%) does significant OH concentration occur. Thus at short times ($t < 100$ μs), it is possible to identify the mixtures that will support combustion by the increased OH ..lorescence intensity and at longer times, by the appearance of the PLIF image alone.

Near the flammability limit for this experiment, we observe the formation of delicate flame fronts which show characteristics of ignition, but are ultimately unable to support combustion. One of the strengths of the time resolved PLIF imaging techniques is that such near limit events can be observed without perturbation. Figure 8 displays a time series of OH PLIF images for a marginally nonigniting mixture of 6% hydrogen. This figure clearly shows the development of a weak flame front 300 μs after the ignition laser. However, the regions of strong OH signal are disconnected and the flame front appears elongated in comparison to the fully igniting 10% results of Fig. 5. By 900 μs, flame has nearly extinguished, and at 2000 μs, no OH signal is detected.

Figure 9 summarizes the time dependence of the spatially integrated OH PLIF signal as a function of hydrogen concentration for three delays after the ignition laser pulse: 100, 300, and 900 μs. At 100 μs, the integrated OH intensity is relatively flat up to 8% where it begins to rise. For times longer than 100 μs, the OH laser-induced-fluorescence signal becomes rapidly weaker for the more dilute mixtures ($< 6\%$ hydrogen) while increasing dramatically for higher concentrations ($> 6\%$ hydrogen). The time dependence of the integrated signals are interesting. For dilute nonignitable mixtures, OH is produced by the spark and promptly decays. The OH signal recorded at longer times extrapolates to a value of zero at about 4%–6 vol.% H_2, which corresponds closely to the lean flammability limit for hydrogen flames.

DISCUSSION

The process of ignition results from the rapid deposition of energy into a gas mixture and can occur by a variety of means such as laser photochemistry, laser absorption, energy transfer, plasma injection, heating, and sparks. Of these, spark ignition is unique as a point source within a gas. A simple view of spark ignition is to consider localizing a sufficient amount of energy within a minimum flame volume to form a flame kernel. The energized gas volume is formed far from equilibrium with its surroundings, having a higher temperature and pressure. The resulting relaxation of the overpressure by expansion of the spark kernel

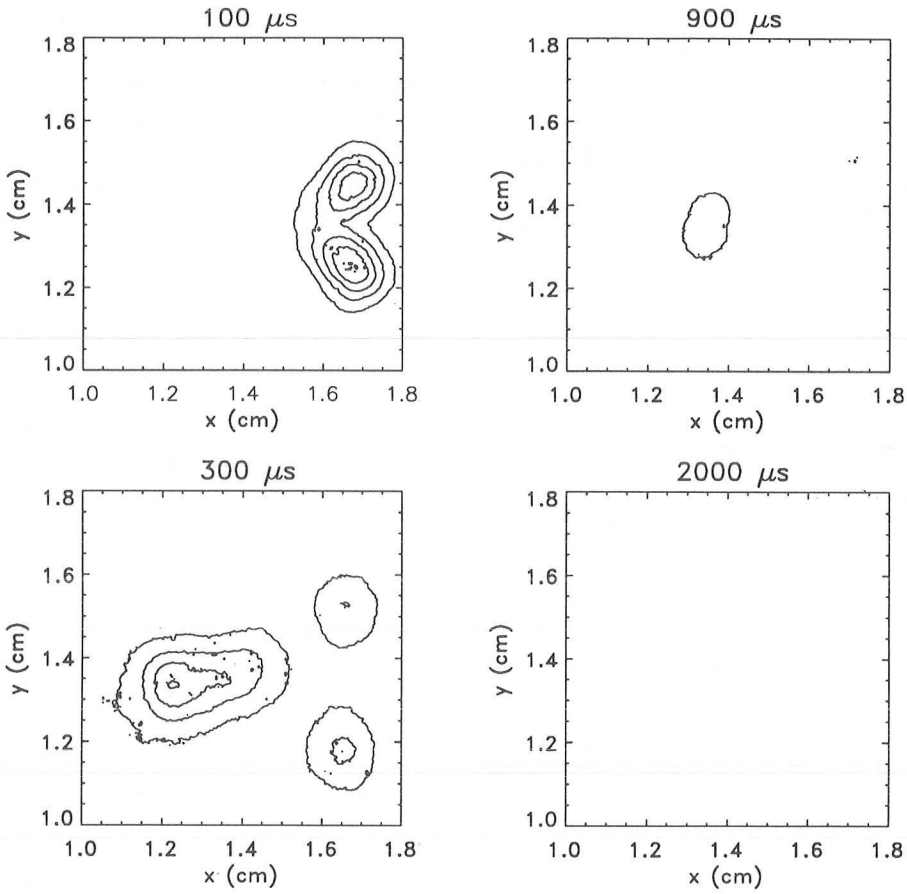

Fig. 8. Contour plots derived from OH PLIF images of laser-ignited mixtures of 6% hydrogen in oxygen/argon synthetic air. The frames depict the development and subsequent extinguishment of a nonigniting flame kernel. No OH is detected at 2000 μs. The contours are linear steps in OH PLIF signal, and the same scaling is used for each panel.

causes mixing and some entrainment of the surrounding gas. If energy deposition is rapid compared to the local speed of sound, which is typical for a laser-induced spark, expansion ensues that causes a shock wave to emanate from the region of the spark kernel. A reaction wave follows the shock wave and leaves behind hot combustion products in the interior. The layer of hot reacting gas surrounding this core reacts with the surrounding gas, releasing more heat and causing further expansion of the flame kernel and entrainment of more ambient gas. Other factors, including thermal conduction and transport of reactive species across the boundary between hot and cold gases, also contribute toward further expansion of the flame kernel and ultimately to flame propagation. If the rate of kernel energy production is greater than the combined rate of kernel energy consumption plus dissipation by dilution and conduction, the flame will ignite. If not, the ignition kernel will extinguish.

The rate of laser energy deposition in this work ($\sim$ 1 mJ/ns) constitutes a rapid ignition. Although the total energy deposited of about 10 mJ significantly exceeds the minimum ignition energy for mixtures with greater than 4% hydrogen [22, 32], ignition in hydrogen/oxygen/argon mixtures only occurs when the hydrogen exceeded 7% of the total gas. Previous laser ignition studies have also noted higher minimum ignition energies for laser ignition of a given gas mixture than for correspondi- electric discharge-induced ignition [22–24]. We offer several possible explanations for this discrepancy. First, the volume encompassed by

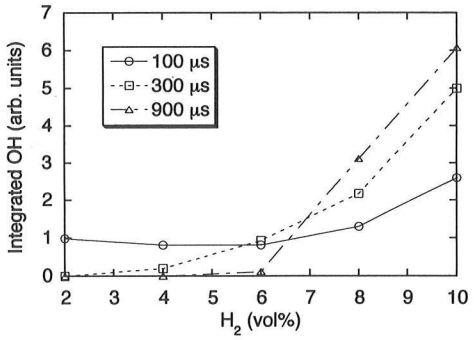

Fig. 9. Spatially integrated total OH PLIF signal as a function of hydrogen concentration and delay time between the ignition laser pulse and the probe laser pulse. Each point is the average of at least four PLIF image integrations to reduce variations due to spark energy and geometry. Note that at 100 μs there is only a weak dependence of the total OH production on hydrogen concentration (see also Fig. 6). By 300 μs, OH production shifts strongly towards the higher concentrations (see Fig. 7). At 900 μs, only the mixture which lead to successful burner ignitions, those above 6% hydrogen, show any significant OH.

the laser-induced sparks may not be optimal for achieving ignition with a minimum energy. The result is that a larger amount of energy is required to achieve the minimum ignition energy *density* throughout a volume larger than the minimal flame volume [24]. A second contribution to the high thresholds for laser spark ignition may be the energy lost via the shock wave that results from the initial expansion of the ignition kernel. This shock wave can disperse energy to the surroundings reducing the energy density within the ignition kernel [22, 23]. As we will discuss below, this shock also affects the size and geometry of the ignition of the ignition kernel and can result in energy densities that are lower than expected. Alternatively this discrepancy may be due to experimental difficulties in electric discharge ignition studies. As discussed in our earlier work, the laser-induced spark minimum ignition energies are in better agreement with simple thermodynamic and kinetic heating calculations, thus raising the possibility that electric discharge ignition process may involve a catalytic interaction with the electrode surfaces [22]. Thus the minimum ignition energies derived from electric discharge experiments may not represent the adiabatic gas phase value [36].

Dynamics of Laser-Induced Sparks

Here we examine properties of the laser-induced spark and coupling of the spark to the ignition process. The energy deposited into a focal volume by a modest laser-induced spark can create instantaneous temperatures and pressures approaching 10^5 K and 10^3 atm, respectively. These extreme conditions relative to the surrounding ambient gas give rise to rapid expansion and dissipation of energy. In previous work, we modeled this process by a simple Taylor blast wave model [22]. In this work we wish to extend the treatment to address two important questions: (i) what is the time scale and spatial extent of the shock expansion, and (ii) how is the deposited spark energy spatially distributed in the expansion. The expressions for a spherical blast wave expansion are given by [37, 38]

$$r = (E_k/\rho_0)^{1/5} t^{2/5}, \tag{3}$$

$$v = \frac{2}{5}(E_k/\rho_0)^{1/2} r^{-3/2}, \tag{4}$$

$$P = [2/(\gamma + 1)]\,\rho_0 v^2, \tag{5}$$

$$T = T_0\left[\left(1 - \frac{v_0^2}{v^2}\right)\left(\frac{\gamma - 1}{\gamma + 1}\right) + 1\right] \times\left[\left(\frac{v^2}{v_0^2} - 1\right)\left(\frac{\gamma - 1}{\gamma + 1}\right) + 1\right], \tag{6}$$

where r is distance, E_k is the thermal energy behind the blast front generated by the spark, ρ_0 is the gas density, v and v_0 are the shock and sonic velocities, respectively, $\gamma = c_p/c_v$, and P and T are the pressure and temperature at the blast front.

Figure 10 shows the temporal evolution of r, v, P, and, T for a 10-mJ spark deposited in a stoichiometric $H_2/O_2/Ar$ mixture. (The calculated difference between stoichiometric and lean mixtures is minor). Results are presented in the absence of dissociation (calculated directly from Eqs. 3–6) and in the presence of dissociation (obtained by adding a kinetic model described shortly). In both cases, the expansion becomes subsonic ($v < 3 \times 10^4$ cm/s) in less than 5 μs for a 10-mJ pulse indicating that the shock wave decays well be-

fore the ignition time for combustion. Hence, there is a distinct separation of time scales between the spark blast wave and the combustion wave. The temporal evolution of a blast wave expansion without dissociation has been considered for a wider range of initial conditions in a previous paper [22].

We now examine the spatial distribution of the spark energy following the blast wave expansion. Two models for the deposited spark energy are considered: (i) a hot gas consisting only of thermal energy E_k of the molecular gas and (ii) a hot gas consisting of thermal energy and potential energy V due to molecular dissociation. In the former case, all the energy is used to propel the expansion and is, therefore, dissipated over a spatial dimension much greater than the minimum flame volume. One would expect inefficient flame ignition under these conditions. In the latter case, energy is stored or localized in the region where dissociation is extensive. Energy storage will be greatest in regions where heating is greatest, namely near the origin of the spark. The localization of energy in the form of radicals should enhance the ignition process. The storage of potential energy V by dissociation also lowers the instantaneous temperature of the hot spark as evident in Fig. 10.

In order to model the spatial dependence of energy storage by dissociation, we add a simple kinetic model to the blast wave equations that considers dissociation of H_2 and O_2. The rate of energy deposition into dissociation is obtained from the following equations

$$k_i(t) = \sum_j k_{ij}(t)c_j = \sum_j A_{ij}T(t)^{n_{ij}} exp\{-E_{a,ij}/k_bT(t)\}c_j, \tag{7}$$

$$\frac{dc_i}{dt} = -k_i(t)c_i, \tag{8}$$

$$\frac{dV}{dt} = -\frac{dE_k}{dt} = -\sum_i D_i\frac{dc_i}{dt}. \tag{9}$$

The first-order rate constant k_i for collisional dissociation of molecule $i = H_2$ and O_2 is obtained from the second-order rate constants k_{ij} for collision partners $j = H_2$, O_2, and Ar, which is expressed by the modified Arrhenius equation in Eq. 7, where A_{ij} is the preexponential factor, n_{ij} is an empirical parameter, $E_{a,ij}$ is the activation energy for dissociation, D_i is the dissociation energy, and c_i is concentration. We have chosen parameters in Eq. 7 given by Cohen and Westberg [39] and Tsang and Hampson [40] in which $E_{a,ij} = D_i$. $T(t)$ is governed by the blast wave expression in Eq. 6. The energy density (energy per unit volume) is calculated by numerical integration of Eqs. 3–9 as a function of time for a fixed spatial grid size Δr corresponding to the width of the blast wave front. This value is estimated to be about 0.01 cm based on measured images of the initial spark radius. The integration interval is given by $\Delta k/v(t)$. The potential energy removed by dissociation over each interval Δt is calculated from the expression

$$\Delta V(t) = \sum_i D_i c_i^0[1 - \exp\{-k_i(t - \Delta t)\Delta t\}], \tag{10}$$

where is ambient concentration. The remaining thermal energy is then $E_k(t) = E_k(t - \Delta t) - \Delta V(t)$. The average energy $< E_k > = [E_k(t) + E_k(t - \Delta t)]/2$ is then used to calculate $r(t)$ and $T(t)$, which in turn are used to calculate $\Delta V(t + \Delta t)$ and $E_k(t + \Delta t)$ for the next time interval.

The spatial distribution of the energy density $\varepsilon(r, t)$ for specific time t after the spark is obtained from the expression

$$\varepsilon(r,t) = \frac{3}{4\pi}\left[\frac{\Delta V(r)}{r^3} + \frac{E_k(t)}{r_b^3(t)}\right], \tag{11}$$

where $r_b(t)$ is the blast wave radius at time t. It is assumed that E_k has a constant value for $r \le r_b$ and is zero outside of the blast wave. A constant E_k is based on the assumption of a uniform pressure behind the shock front, in which case the thermal energy density is constant within the shock front (i.e., $P = nRT/V$). Calculated energy density distributions are plotted in Fig. 11 for increasing values of t. the absence of dissociative energy storage, energy density appears in Fig. 11a as a series of steps that diffuse with increasing time. In the

presence of dissociation, energy localization is evident in Fig. 11b. Energy storage occurs when the rate of dissociation is comparable to or greater than the rate of cooling. As the blast wave expansion progresses, the thermal energy density remaining for dissociation decreases until dissociation becomes insignificant. Because of the exponential dependence of k_i on T, the boundary marking regions of significant and insignificant dissociation is rather sharp as seen in Fig. 11b. An expanded view of this boundary is plotted in Fig. 11c for the relative concentration of dissociated and undissociated H_2 and O_2. The size of the energy storage region is consistent with the size of an early spark as measured in the first panel of Fig. 3. The dip in energy density toward the spark origin in Fig. 11b is due to the very high velocity of the blast wave. In this simple model, the high temperature of the early blast wave, which favors dissociation, is more than offset by the high velocity, which shortens the exposure time of the gas to the blast wave front. We have refrained from presenting data close to the origin where the temperatures are well outside the valid range of the kinetics parameters used (600–5000 K for H_2 dissociation [39], whereas the blast wave temperature is calculated to be 10^5 K at a radius of 0.024 cm). So it is uncertain whether the energy dip at the origin is a real phenomena. Outside of the dissociation region, the remaining thermal energy dissipates by expansion, however, the stored energy remains for some indefinite time that depends on mixing and cooling mechanisms not considered in this model.

The simple kinetic model adapted to the blast wave equations serves to illustrate the mechanism of energy storage by dissociation and the role that it might play in the efficiency of laser-induced spark ignition. However, to keep the model sufficiently elementary to visualize the pertinent physical mechanism, important simplifications have been made. These include (i) not allowing the stored energy to expand due to pressure gradients following the blast wave, (ii) ignoring the thermal energy increase from the increase in particle density due to dissociation (this contribution is small relative to the potential energy due to pressure gradients), (iii) using a fixed value of the blast wave width Δr for the integrating grid size, (iv) ignoring the pressure dependence of k_i, and (v) using an unrealistically small number of reactions. To test the chemical part of our dissociative energy storage model, we ran zero-dimensional chemical kinetics calculations using the CHEMKIN kinetics package [41] with a 27 step H_2/air reaction mechanism taken from Thorne et al. [42]. Ten millijoules of energy was deposited into the same gas mixture in the form of ionization and the resultant heat generated by ion–electron recombination [43] was observed to dissociate the majority of H_2 and O_2. OH is a minor constituent at these early times. Our kinetics modeling program is not currently equipped to handle the spark expansion so the spatial extent of dissociation could not be tested. However, the calculated thermal energy available to expansion and the relative yield of dissociation calculated by the two models are sufficiently similar that a more realistic treatment of the chemistry should not alter the results greatly. We expect a much greater effect on the calculated results by including a realistic treatment of the gas dynamics in place of the blast wave model. We are developing a more sophisticated model for calculating the spatial distribution of energy and are recording detailed images of spark propagation in order to understand the energy dynamics of laser-induced sparks.

Dynamics of Flame Propagation

Focusing on the geometries of the nascent flame kernels, we can readily distinguish two physical developments. At short times ($t < 100$ μs), the flame fronts rapidly develop toward toroidal geometry (see Fig. 3). The general shape of the expansion resembles closely the shapes obtained using Schlieren photography to image ignition kernels following electric discharge ignitions [12–14, 33–35]. At longer times ($t > 100$ μs), the flame front propagates back toward the ignition laser (see Fig. 5). This phenomenon is believed to be unique to laser ignition studies, and has been observed only once previously by Hanson and coworkers for a laser-ignited methane/air flame [20]. Because theoretical methods are not yet capable of

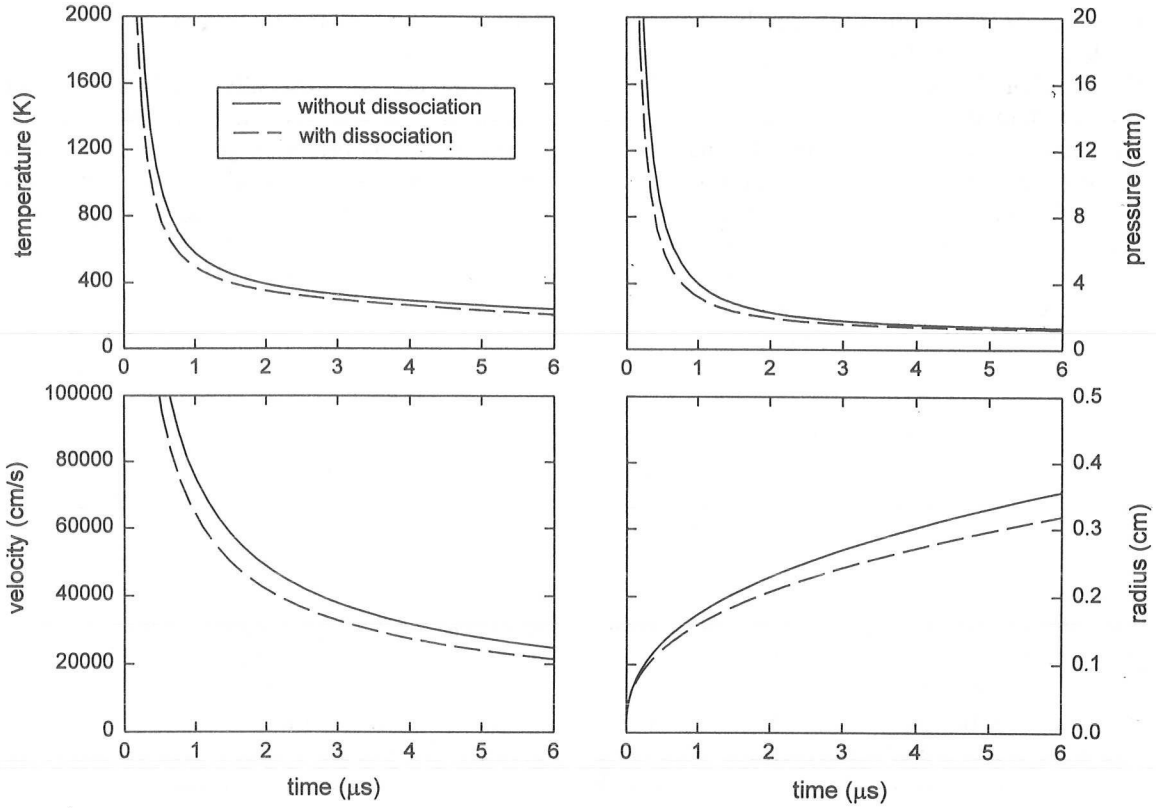

Fig. 10. Properties of an expanding laser-induced spark for a 1-atm stoichiometric $H_2/O_2/Ar$ mixture. Input energy is 10 mJ. See text for discussion of the dissociation model.

describing these two complex phenomena together, we will consider them separately for the purposes of this discussion and reconcile the two thereafter.

Short time, toroidal flame front development appears to be a universal phenomenon of spark ignitions. Results of a recent computer simulation by Kono et al. provide us with some important insights into this process [12]. This two dimensional calculation simulated the aftermath of a cylindrically symmetric, instantaneous electric discharge (less than a few microseconds) in nitrogen and neglected chemical contributions. The results of this study show convincingly that the toroidal shape results directly from the passing of the shock wave, emanating outward from the region of the discharge at a very high velocity. We present a visualization of this phenomena in Fig. 12. This shock wave clearly separates from the initial nucleus after only a few microseconds and results in an overexpansion of the ignition kernel, inducing an inward flow along the axis of the cylindrical spark toward the center. At the center, the opposing gas flows collide and deviate outward from the center, creating a pair of cylindrically symmetric vortices. This flow of gas causes the development of the torus. Because these events occur in the absence of chemical reactions, they lead to similar shapes of the ignition kernels regardless of the constituents of the gas. Figure 6 shows this clearly in a series of PLIF images taken at 100 μs with hydrogen concentrations of 2%–8%. Clearly, the toroid geometry evidenced by these frames are nearly independent of the gas constitution. For $t \geq 100$ μs, even mixtures that do not ignite show this toroidal geometry. This is consistent with the development of the torus being a phenomenon due not to the chemical heat release of combustion, but instead to the discharge shock wave.

The long time propagation of the flame backwards along the path of the ignition laser

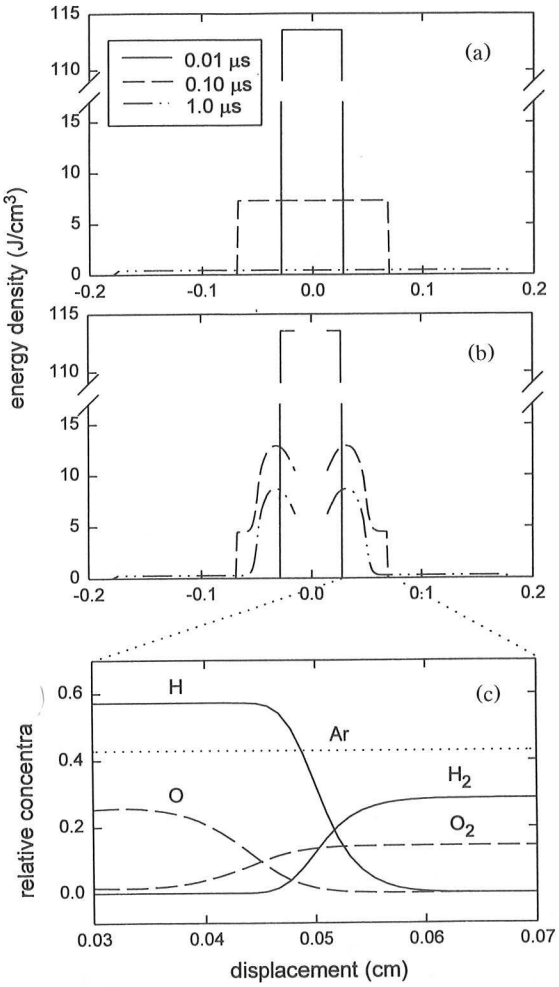

Fig. 11. Calculated energy density as a function of displacement from spark origin for various times after initiation. (a) no dissociation leads to complete dissipation of the energy in the blast wave expansion, (b) H_2 and O_2 dissociation leads to localization of energy in the vicinity of the initial spark. Displacement refers to a linear coordinate through the spark origin. The blast wave is assumed to have spherical symmetry. Arrhenius-type kinetics parameters were obtained for collisional dissociation of H_2 with collision partners H_2, Ar, and N_2, the latter being used for collisions with O_2 [38]. Parameters for dissociation of O_2 could only be found for Ar as a collision partner [39], so other dissociative collisions were ignored in the calculation. (c) An expanded view of the boundary region at 1 μs where the extent of dissociation changes abruptly.

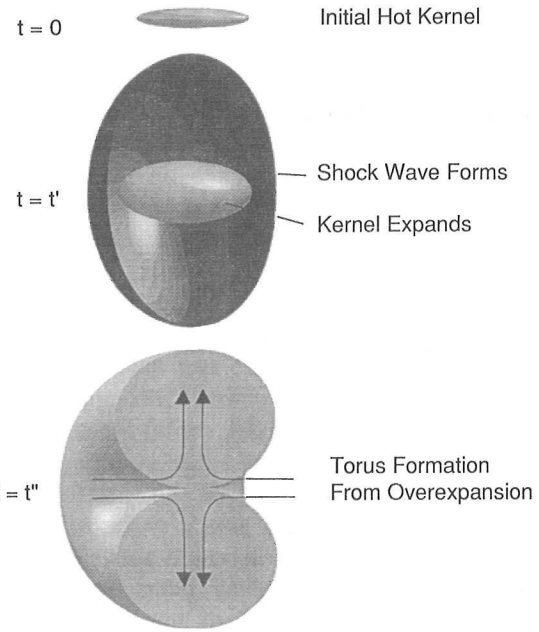

Fig. 12. Diagram explaining the development of a toroidal flame kernel following laser ignition after Kono et al. [12]. Top: initial spark kernel has elevated temperature and pressure embedded in a cooler, less dense environment. Middle: the initial kernel relaxes via an expansion that leaves it at elevated temperature but at reduced pressure. A shock wave results from the rapid expansion that propagates rapidly, separate from the development of a flame. Bottom: the rapid relaxation of the plasma results in a slight over-expansion, inducing a flow of gas from the ends inward toward the center. This flow pushes outward radially, creating a toroidal shape.

beam is more difficult to explain. This phenomenon may be related to the initial flow field created by the spark. Ramsden and Davies first observed that the plasma generated by laser breakdown propagates backward toward the spark laser [45]. This so-called radiation transport wave is due to dynamical process of laser-induced breakdown. In the generally accepted model [46], an initial plasma is formed near the focus of the laser. This plasma rapidly heats the surrounding gas, ionizing it. The freshly ionized gas on the side facing the laser then is able to absorb more laser energy through the inverse bremsstrahlung mechanism and is rapidly heated. Thus the boundary of highly heated plasma rapidly propagates back toward the spark laser. A net velocity of approximately 10^7 cm s^{-1} is produced in the direction of the laser. Although this velocity will likely be damped in the approximately 100-μs delay between the spark and ignition, it is more than five orders of magnitude larger than the adiabatic flame speeds for our mixtures (< 70 cm s^{-1}). Thus the radiation trans-

port wave will likely create a sufficiently long-lived velocity component toward the spark laser to produce the observed anisotropic propagation of the combustion wave. Therefore the mechanism of energy deposition for ignition may have a strong influence on the resulting combustion wave.

A second possible explanation requires a significant asymmetry to the spark with a corresponding asymmetry in the gas flow that follows propagation of the shock wave and ensuing overexpansion. The laser-induced sparks clearly provide this asymmetry through the formation of an intense spark center located away from the midpoint of the spark volume, biased towards the spark laser (see the first frame in Fig. 4). The resulting shock wave will then propagate outward as discussed above but with an axial component away from the intense spark center and therefore toward from the direction of the spark laser. Gases rushing to fill the hot, over-expanded region then quickly ignite to form the kernels observed. The motion of the flame front away from the center of the ignition volume indicated in Figs. 4 and 5 provides evidence of an asymmetric combustion wave participating in the formation of the flame, although it could be induced by the spark formation process described above or by convective currents emanating from the flame front that is forming at the left of the figures.

An additional contributing factor to the asymmetry evidenced in Figs. 3–8 may be the preheating of the gases by the focused laser beam that ignites the gases. This preheated gas readily ignites resulting in a flame front that propagates much more quickly than it would through cold gas. Below we discuss evidence of this in terms of the flame front velocity of the ignition kernel. The extent of preheating by the laser beam depends on the focusing characteristics of the ignition laser beam, the optical properties of the gas, and the amount of energy absorbed by the spark. The observed anisotropic flame shapes may well arise from a combination of laser-induced gas dynamics and laser heating.

An important point is that propagation back toward the ignition laser occurs only in mixtures that fully ignite and that it becomes the predominate feature at long times. Clearly this feature is indicative of ignition. Thus an induction period of approximately 50–100 μs must exist before ignition. The appearance of the toroidal structure in this period, as Kono et al. have shown [12], is due to hydrodynamic effects and appears to be largely separable from the final ignited flame front. The pronounced anisotropy of the later flame front may have some practical use since it provides the opportunity to direct the initial velocity of the combustion wave in a reproducible manner over distances of at least 1 cm.

Adiabatic flame speeds for hydrogen in air range from over 250 cm/s when hydrogen accounts for 40%–50% of the gas down to approximately 70 cm/s at the 20% hydrogen level [32]. For our Ar/O_2 mixtures, the flame speeds are expected to be approximately a factor of 1.3 higher due to the lower heat capacity of Ar. All flames used in our experiments have hydrogen concentrations below 11% where no experimental measurements a available. Given the 10.4-cm/s flow velocity and steep decrease of flame speed with hydrogen concentration, some of these flames might be expected to simply have insufficient hydrogen to permit propagation of the nascent flame down to the surface of the burner where a flame would stabilize. Thus we might be tempted to explain the lack of ignition observed in mixtures with less than 7% hydrogen as a flame blow off. However, as shown in Figs. 7–9, these flame kernels begin to die out after only 300 μs. Because the bulk gas flow is essentially stagnant at these short times (moving about 0.03 mm), flame speed relative to the velocity of the gases is not the issue here. Our only conclusion can be that the ignition kernels contain too little energy per unit volume to ignite mixtures with less than 7% hydrogen gas.

The flame front velocity of the flame kernel may give some insight into the driving mechanism of nascent laser-spark ignited flame propagation. As discussed above, the adiabatic flame speeds of hydrogen in air are less than 250 cm/s and for the dilute mixtures described here, they are expected to be much low (< 70 cm/s). However, Fig. 5 clearly shows a flame front propagating approximately 0.7 cm between 300 μs and 2.00 ms giving an instanta-

neous velocity of about 390 cm/s. This is about an order of magnitude higher than the expected adiabatic flame speed. Indeed in the interval 100–300 μs during which the flame front develops along the laser axis, the velocity is > 1500 cm/s. This velocity is not directly related to the blast wave velocity, which would have expanded to much greater distances on these time scales. Between 2–3 ms, the flame front appears to slow down to < 200 cm/s. The rapid expansion of the flame front at short times must be due to nonequilibrium effects of the spark ignition. These high instantaneous flame front velocities are consistent with the model suggested above in which laser heating of the gas on the ignition laser side of the spark leads to asymmetric flame propagation, since higher initial temperatures lead to higher flame speeds and shorter induction times. The slowing of the flame front by 3 ms may then indicate that it has expanded beyond the preheat zone. This directed, high-velocity flame propagation may be useful as a flame holder in supersonic flow [44, 45]. The rapid expansion of the flame front may also be due simply to expansion of the hot burned gas within the kernel to maintain constant pressure. The deceleration at longer times would then be due to the transition of the flame front from approximately spherical to planar. Subsequent experiments will test for this by systematically varying the ignition laser energy over a large range than is possible with our current small ignition laser. This should enhance any preheating effects without changing the gas expansion effects.

CONCLUSIONS

In this work, we have presented time-solved images of expanding flame kernels initiated by laser-induced sparks in $H_2/O_2/Ar$ mixtures. PLIF imaging of the OH produced in the nascent flame provides a time and space resolved, diagnostic probe of flame kernel ignition or extinction. Consistent with theories presented by Kono et al., the initial ($t < 100$ μs) outward growth of the kernel produces a torus that correlates with shock front propagation and is independent of flame ignition. As a dynamical phenomenon and not a chemical phenomenon, the diameter of the torus is nearly independent of gas constitution. The primary difference evidenced between PLIF images of mixtures that ignite and those that do not is the intensity of the OH emission and the appearance of significant kernel growth back toward the spark laser at times > 100 μs after the spark laser pulse.

Flame kernels that dissipate without ignition yield little PLIF intensity after 100 μs while images of flame kernels in ignitable mixtures have significantly more intensity and display reproducible structure. Flame kernels that ignite tend to propagate back toward the spark laser, most likely the result of a high degree of laser preheating, although there may be some contribution from a shock wave phenomenon that results from a biased distribution of energy in the velocity of the laser-induced spark. This anisotropy in the initial flame propagation is unique to laser ignition and provides the opportunity to direct the initial propagation of the flame front in a predetermined direction over macroscopic distances (at least 1.0 cm) at high instantaneous flame speeds.

Future experiments in this laboratory will exploit the wealth of information available from PLIF imaging of laser ignited flame kernels to study flame growth and suppression in flammable mixtures doped with halon and halon replacement candidate fire suppressants. These experiments should provide valuable insight into the basic physics and chemistry of fire suppressants. In conjunction with these studies, we plan to extend our PLIF imaging capabilities to include other radicals critical to combustion and suppression such as hydrogen, oxygen, and bromine atoms.

This work was supported by the Aerospace Sponsored Research Program and the USAF / SMC Division of Environmental Management. The authors would like to thank Prof. Paul Ronney for valuable discussions.

REFERENCES

1. Laster, W. R., and Sojka, P. E., *J. Propulsion* 5:385–390 (1989).
2. Westbrook, C. K., *Nineteenth Symposium (International) on Combustion,* The Combustion Institute, Pittsburgh, 1982, pp. 127–141.

3. Ballal, D. R., and Lefebvre, A. H., *Combust. Flame* 35:155–168 (1979).
4. Ballal, D. R., and Lefebvre, A. H., *Proc. R. Soc. Lond.* 357:163–181 (1977).
5. Levy, M. E., Cerkanowicz, A. E., and McAlevy III, R. F., AIAA Seventeenth Aerospace Sciences Meeting, paper 69–88, January 1969.
6. Dixon-Lewis, G. and Shepherd, I. G., *Fifteenth Symposium (International) on Combustion,* The Combustion Institute, Pittsburgh, 1974, pp. 1483–1491.
7. Sher, E., and Refael, S., *Nineteenth Symposium (International) on Combustion,* The Combustion Institute, Pittsburgh, 1982, pp. 251–257.
8. Wiriyawit, S., and Dabora, E. K., *Twentieth Symposium (International) on Combustion,* The Combustion Institute, Pittsburgh, 1984, pp. 179–186.
9. Sloane, T. M., and Schoene, A. Y., *Twenty-Second Symposium (International) on Combustion,* The Combustion Institute, Pittsburgh, 1988, pp. 1669–1679.
10. Schmieder, R. W. *J. Appl. Phys.* 52:3000–3003 (1981).
11. Lutz, A. E., Kee, R. J., Miller, J. A., Dwyer, H. A., and Oppenheim, A. K., *Twenty-Second Symposium (International) on Combustion*, The Combustion Institute, Pittsburgh, 1988, pp. 1683–1693.
12. Kono, M., Niu, K., Tsukamoto, T., and Ujiie, Y., *Twenty-Second Symposium (International) on Combustion,* The Combustion Institute, Pittsburgh, 1988, pp. 1643–1649.
13. Maly, R., and Vogel, M., *Seventeenth Symposium (International) on Combustion,* The Combustion Institute, Pittsburgh, 1978, pp. 821–831.
14. Borghese, A., D'Alessio, A., Diana, M., and Venitozzi, C., *Twenty-Second Symposium (International) on Combustion,* The Combustion Institute, Pittsburgh, 1988, pp. 1651–1659.
15. Behrendt, F., Goyal, G., Mass, U., and Warnatz, J., *Twenty-Fourth Symposium (International) on Combustion,* The Combustion Institute, Pittsburgh, 1992, pp. 83–91.
16. Dyer, M. J., and Crosley, D. R., *Opt. Lett.* 7:382–384 (1982).
17. Kychakoff, G., Howe, R. D., Hanson, R. K., and McDaniel, J. C., *Appl. Opt.*21:3225–3227 (1982).
18. Seitzman, J. M., and Hanson, R. K., in *Instrumentation for Flows with Combustion*, Academic Press, New York, 1993, pp. 405–466.
19. Arnold, A., Becker, H., Suntz, R., Monkhouse, P., Wolfrum, J., Maly, R., and Pfister, W., *Opt. Lett.* 15:831–833 (1990).
20. Seitzman, J. M., Paul, P. H., and Hanson, R. K., Paper 88-2775, AIAA Thermophysics, Plasmadynamics and Lasers Conference, San Antonio, TX, 1988.
21. Ronney, P. D., *Opt. Eng.* 33:510–521 (1994).
22. Syage, J. A., Fournier, E. W., Rianda, R., and Cohen, R. B. *J. Appl. Phys.* 64:1499–1507 (1987).
23. Weinberg, F. J., and Wilson, J. R., *Proc. Roy. Soc. Lond. A* 321:41–52 (1971).
24. Lee, J. H., and Knystautas, R., *AIAA J.* 7:312–317 (1969).
25. Hill, R. A., and Laguna, G. A., *Opt. Commun.* 32;435–439 (1980).
26. Forch, B. E., and Miziolek, A. W., *Combust. Sci Technol.* 52:151–159 (1987).
27. Forch, B. E., and Miziolek, A. W., *Combust. Flame* 52:254–262 (1991).
28. Miziolek, A. W., and Sausa, R. C., BRL Technical Report BRL-TR-2644, 1985.
29. Lavid, M., and Stevens, J. G., *Combust. Flame* 60:195–202 (1985).
30. Chou, M-S., and Zukowski, T. J., *Combust. Flame* 87:191–202 (1991).
31. Maas, U., Raffel, B., Wolfrum, J., and Warnatz, J., *Twenty-First Symposium (International) on Combustion,* The Combustion Institute, Pittsburgh, 1986, pp. 1869–1876.
32. Lewis, B. and Von Elbe, G., *Combustion, Flames, and Explosion of Gases,* 2nd ed., Academic, New York, 1967, pp. 351ff.
33. Strehlow, R. A., *Combustion Fundamentals,* McGraw-Hill, New York, 1985.
34. Maly, R., *Eighteenth Symposium (International) on Combustion,* The Combustion Institute, Pittsburgh, 1980, p. 1747–1754.
35. Sloane, T. M., and Ratcliffe, J. W., *Chemistry Combustion Processes* (ACS Symposium Series 249, American Chemical Society, New York, 1984), p. 205–222.
36. Sloane, T. M., and Ronney, P. D., *Combust. Sci Techno.* 88:1–13 (1992).
37. Davies, R. M., and Taylor, Sir G., *Proc. Roy. Soc. A* 200:375–390 (1950).
38. Taylor, Sir G., *Proc. Roy. Soc. A* 201:175–186 (1950).
39. Cohen, N., and Westberg, K. R., *J. Phys. Chem. Ref. Data* 12:531 (1983).
40. Tsang, W., and Hampson, R. F., *J. Phys. Chem. Ref. Data.* 15:1087 (1986).
41. Kee, R. J., Rupley, F. M., and Miller, J. A., Sandia Report, SAND89-8009.UC-401, 1989.
42. Thorne, L. R., Branch, M. C., Chandler, D. W., Kee, R. J., and Miller, J. A., *Twenty-First Symposium International) on Combustion,* The Combustion Institute, Pittsburgh, 1986, pp. 965–977.
43. Biondi, M. A., in *Defence Nuclear Agency Reaction Rate Handbook,* 2nd ed. (DOD Nuclear Information and Analysis Center, Santa Barbara, 1983), 16.1–16.36.
44. Carrier, G. F., Fendell, F. E., McGregor, R., Cook, S., and Vazirani, M., *J. Prop. Power* 8:472–480 (1992).
45. S. A. Ramsden and W. E. R. Davies, *Phys. Rev. Lett.* 13, 227–229 (1964).
46. C. DeMichelis, IEEE *J. Quantum Electron.* QE-5:188–202 (1969).

Received 28 February 1994; revised 14 December 1994